Research Article Vol. 15, No. 2 / 1 Feb 2025 / Optical Materials Express 164
Optical Materials EXPRESS

Enhanced near-infrared absorption in lattice-matched $Sc_{0.14}Al_{0.86}N$/GaN multi-quantum wells: growth optimization and insights into polarization parameters

Zain Ul Abdin,[1,2,†] Govardan Gopakumar,[1,2,†] Rajendra Kumar,[1,2,†] Michael J. Manfra,[1,2,3,4] and Oana Malis[1,2,*]

[1]Department of Physics and Astronomy, Purdue University, West Lafayette, Indiana 47907, USA
[2]Birck Nanotechnology Center, West Lafayette, Indiana 47907, USA
[3]School of Materials Engineering, Purdue University, West Lafayette, Indiana 47907, USA
[4]School of Electrical and Computer Engineering, Purdue University, West Lafayette, Indiana 47907, USA
[†]These authors contributed equally.
[*]omalis@purdue.edu

Abstract: We report on the near-infrared intersubband (ISB) absorption properties of strain-free $Sc_{0.14}Al_{0.86}N$/GaN multiple quantum wells (MQWs) grown on c-plane GaN substrates by molecular beam epitaxy. These MQWs exhibit strong, sharp, and tunable absorption energies between 515 meV and 709 meV, for well widths ranging from 7 nm to 1.5 nm, respectively. Observation of ISB absorption in ultra-thin $Sc_{0.14}Al_{0.86}N$/GaN MQWs not only extends the near-infrared range accessible with Sc-containing nitrides but also highlights the challenges of growing nanometer-thick GaN quantum wells. We explore the effects of growth temperature on absorption characteristics and find that substrate temperatures above 600°C significantly enhance ISB absorption intensity but also introduce an energy redshift for the narrowest wells. The redshift is attributed to increased interface roughness due to ScAlN surface morphology degradation at higher temperatures. Additionally, a comparison of experimental results with simulated band-structures indicates that the magnitude of net polarization rises faster with Sc-composition than previously suggested by theoretical calculations. This study advances the prospects of ScAlN/GaN heterostructures for novel photonic devices in the technologically important near-infrared range.

© 2025 Optica Publishing Group under the terms of the Optica Open Access Publishing Agreement

1. Introduction

Sc-aluminum-nitride alloys have introduced novel characteristics to the well-researched III-nitride semiconductor system [1], extending their capability for future quantum electronic technologies and non-linear optics [2–5]. The III-nitride semiconductors, known for their wide and tunable bandgap, strong polarization effects, and high chemical stability, are essential for modern technology [6]. The tunable bandgap of III-nitrides makes them extremely attractive for optoelectronic applications, such as light-emitting diodes (LEDs) and laser diodes, covering a spectrum from visible to ultraviolet wavelengths [7–9]. Due to their wide bandgap, III-nitrides can handle high voltages and currents while maintaining high efficiency, making them ideal for power electronics. III-nitrides are also widely used in high-frequency electronic devices because of their ability to maintain performance at high temperatures and under high power conditions [10,11]. Moreover, due to large conduction band offsets and large longitudinal-optical phonon energy, the III-nitrides are promising for infrared devices such as quantum well infrared photodetectors (QWIPs) and quantum cascade lasers (QCLs) [12–17].

Infrared optoelectronic devices often utilize optical transitions between quantized energy levels in the conduction band of heterostructures made of semiconductors of different bandgaps [18].

#545820 https://doi.org/10.1364/OME.545820
Journal © 2025 Received 22 Oct 2024; revised 20 Nov 2024; accepted 21 Nov 2024; published 6 Jan 2025

Optical Materials EXPRESS

These intersubband devices typically consist of multi-quantum well structures to enhance optical transition strength. The quantized energy levels are determined by the periodic quantum well (QW) potential formed by the conduction band alignment between the two materials: a lower bandgap material for the wells, and a higher bandgap material for the barriers. Therefore, the intersubband transitions (ISBT) can be widely tuned by adjusting the conduction band profile, primarily through layer thickness and material composition. Conduction band offsets (CBOs) determine the depth of the QWs and eventually limit the energy of the ISB transitions [12]. III-nitride heterostructures offer substantial CBOs, around 2.1 eV between $Sc_{0.14}Al_{0.86}N$ and GaN [19], making them ideal candidates for ultrafast devices operating in the near-infrared spectrum [13,14,20–23]. Additionally, the high energy of GaN longitudinal optical phonons (>90 meV) opens possibilities for high-temperature ISB devices functioning within the 5–10 THz range [15,24]. However, the advancement of traditional nitride-based ISB devices, such as AlGaN/GaN MQWs, is hindered by the inherent lattice-mismatch among the various nitrides [25–27]. Alongside defects induced by strain, lattice-mismatch results in interface roughening, which compromises the uniformity of layer thicknesses. Consequently, device performance suffers due to broadening and reduction of ISB transitions. Since the epilayers for ISB devices are fairly thick (>100 nm), managing lattice-mismatch is critical for optimizing the performance of nitride-based devices [28,29].

Wurtzite $Sc_xAl_{1-x}N$ overcomes this challenge as it can be lattice-matched to c-plane GaN. ScAlN/GaN heterostructures have emerged as a preferred material platform for devices due to its versatile and unique properties [30–62]. ScAlN possesses desirable characteristics like large bandgap [2,4], large breakdown voltages [28], enhanced polarization [55], and novel ferroelectric properties [38], making it a leading material for modern high-power electronics including high electron mobility transistors (HEMTs) and heterostructure field effect transistors (HFETs) [56–60]. ScAlN's high remnant polarization and robust switching characteristics make it an ideal material system for applications in memristors [61]. Nitride memristors, featuring stable nitrogen vacancies, offer superior cycle performance and structural stability compared to oxide counterparts, potentially revolutionizing memory computing devices by extending lifespan and reducing costs amid current oxide memristor challenges [61]. Moreover, ScAlN has a high Curie temperature, allowing it to maintain its ferroelectric properties at elevated temperatures. ScAlN/GaN heterostructures have exhibited stable on/off states that lasted for months at room temperature and remained stable even at high temperatures (approx. 670 K) [4].

Previous to recent work [29], $Sc_xAl_{1-x}N$ was believed to be lattice-matched to GaN at approximately $x = 0.18$. Starting from this assumption, we previously investigated ISB transitions in wurtzite $Sc_{0.18}Al_{0.82}N$/GaN multiple quantum wells on c-plane GaN using near-infrared spectroscopy and computational modeling [62]. The $Sc_{0.18}Al_{0.82}N$/GaN MQW structures exhibited strong and narrow ISB absorption in the range of 645 meV to 518 meV for quantum well widths varying from 2.5 nm to 8 nm, respectively. However, these $Sc_{0.18}Al_{0.82}N$/GaN MQWs showed minimal or no absorption in QWs thinner than 2.5 nm. X-ray diffraction (XRD) reciprocal space mapping analysis of these MQWs revealed evidence of relaxation which likely induced strain-related defects such as misfit dislocations, threading dislocations, and stacking faults. These defects can significantly compromise the optical properties of MQWs [25,26]. A subsequent in-depth XRD study of the microstructure of $Sc_xAl_{1-x}N$ grown on (0001) GaN provided strong evidence that the lattice-matching condition occurs at $x = 0.14 \pm 0.01$, instead of $x = 0.18$ [29].

Building on our previous results [29], this paper focuses on investigating intersubband transitions in lattice-matched, strain-free $Sc_{0.14}Al_{0.86}N$/GaN MQWs grown by molecular beam epitaxy on c-plane GaN substrates. GaN is the well material and $Sc_{0.14}Al_{0.86}N$ is the barrier material. This study aims to extend the range of ISB absorption energies, with a particular focus on the development of ScAlN/GaN MQWs optimized for operation in the technologically

Optical Materials EXPRESS

significant near-infrared range [14,63]. Wurtzite $Sc_{0.14}Al_{0.86}N$/GaN MQWs exhibit exceptional near-infrared ISB absorption, with energies ranging from approximately 515 meV to 709 meV, and with linewidths as narrow as 46 meV. Significantly, this work is the first to report substantial absorption in quantum wells narrower than 2.5 nm, enabling access to higher near-infrared energies. Achieving high ISB absorption energies necessitates the precise growth of ultra-thin nitride layers while maintaining uniformity and abrupt interfaces. We address the challenges associated with enhancing and extending ISB absorption to higher energies and discuss optimization of ScAlN/GaN growth conditions, particularly the growth temperature. Additionally, this study investigates the impact of spontaneous polarization inherent to the wurtzite structure and piezoelectric polarization resulting from lattice-mismatch-induced strain on the band structure of ScAlN/GaN MQWs, and subsequently on ISB transitions. Experimental and simulated ISB transition energies provide direct insights into the fundamental polarization parameters of wurtzite ScAlN. This paper lays crucial groundwork for ISB-based device applications by advancing the understanding of the properties of ScAlN/GaN heterostructures.

2. Experiments and simulations

The $Sc_{0.14}Al_{0.86}N$/GaN heterostructures consist of 50 quantum wells grown using plasma-assisted molecular beam epitaxy (MBE) on commercially available Fe-doped semi-insulating c-plane GaN templates on sapphire (0001) substrates (dislocation density of $8.0 \times 10^8\,cm^{-2}$). The details of all sample design and measurement results are given in the Supplement 1. MBE provides exquisite control over layer thickness, which has been crucial for advancing nitride-based ISB devices [12]. The substrates were first coated with a 1 µm tungsten silicide layer on the backside to enhance thermal coupling with the MBE heater. Before loading the substrates in the MBE chamber, they were cleaned with trichloroethylene, acetone, and methanol to eliminate organic impurities, followed by a 10-minute acid etch in HCl. The substrates were then thoroughly rinsed with deionized water and dried with nitrogen gas. They were outgassed overnight (>12 hours) at 550°C in an ultra-high vacuum chamber connected to the MBE chamber. High-purity Al, Ga (purity 99.99999%), and Sc (purity 99.999% trace rare-earth metals) metal sources were used to minimize impurity-related effects in the MQWs. Active nitrogen was supplied by a Veeco Unibulb RF plasma source operating at 250-305 W forward power, with N_2 flow rate maintained at 0.25-0.50 sccm, resulting in a nitrogen-limited GaN growth rate of ~3.6–8.2 nm/min, respectively. Prior to growing MQWs, a 150 nm GaN buffer layer was grown at 740°C substrate temperature under Ga-rich conditions, producing a smooth GaN surface with a root mean square (rms) roughness of 0.4 nm over a 5 µm × 5 µm area. The MQWs were grown in a range of substrate temperatures between 500°C and 625°C to optimize ISB absorption. The metal-to-nitrogen ratios for the ScAlN and GaN layers in the MQW structure were approximately 0.8 and 1.2, respectively. Silicon doping was introduced through two δ-doping sheets placed 1 nm from each interface during growth pauses, with doping density controlled by the Si-cell temperature. The samples employed Si-cell temperatures of either 1375°C or 1402°C that correspond to nominal sheet electron densities of $8.0 \times 10^{12}\,cm^{-2}$ or $1.6 \times 10^{13}\,cm^{-2}$ per quantum well, respectively.

Structural characterization of the samples was performed using atomic force microscopy, x-ray diffraction, and transmission electron microscopy. High-angle annular dark-field scanning transmission electron microscopy (HAADF-STEM) images were utilized to measure the thickness of individual layers. The HAADF-STEM samples were prepared using a Thermo Scientific Helios G4 UX Dual Beam FIB, followed by cleaning with a Fischione Ar Plasma cleaner to eliminate any contamination from the FIB process or exposure to air. HAADF-STEM imaging and analysis were carried out using a Thermo Scientific Themis Z Double Aberration Corrected S/TEM, operated at an acceleration voltage of 300 kV and screen current of 0.12 nA.

Optical Materials EXPRESS

Symmetric ω-2θ XRD scans were obtained using a Panalytical X'Pert3 MRD system. To estimate the Sc composition in the barrier layers and verify the layer thicknesses, the experimental XRD scans were modeled using the Panalytical Epitaxy software package. This modeling was based on the composition dependence of lattice constants, as determined in our previous research [24]. Additionally, reciprocal space mapping (RSM) of the $(10\bar{1}5)$ reflection was conducted using a Panalytical Empyrean diffractometer to analyze the strain state of the MQW structures. The HAADF-STEM image and RSM plot of a 50-repeat 6 nm GaN, 6 nm $Sc_{0.14}Al_{0.86}N$ MQW structure are shown in Fig. 1. The HAADF-STEM image indicates uniform layers and relatively sharp interfaces. The RSM plot exhibits MQW peaks that are equally spaced in reciprocal space and are also known as superlattice peaks. The RSM also reveals that the $Sc_{0.14}Al_{0.86}N$ layers are coherently strained to GaN.

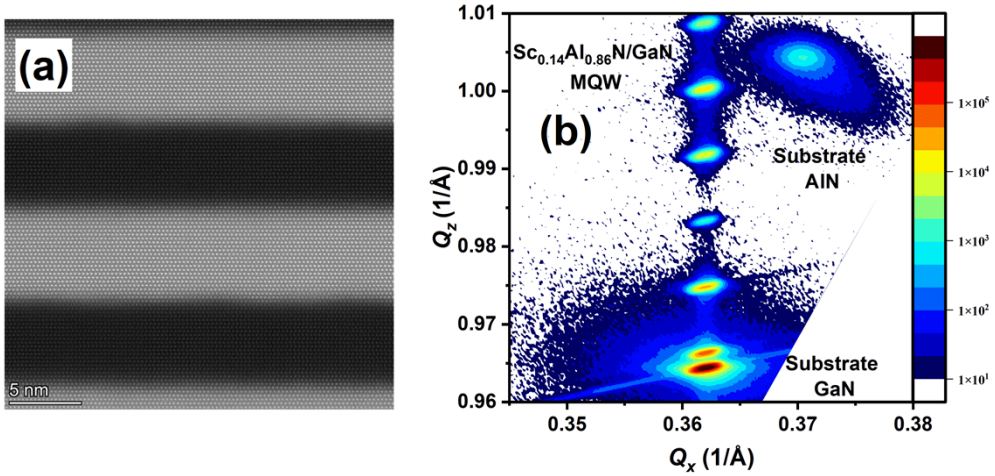

Fig. 1. (a) HAADF-STEM of a $Sc_{0.14}Al_{0.86}N$/GaN (6 nm, 6 nm) MQW heterostructure. Dark regions represent the ScAlN barriers, while light regions are the GaN well layers. (b) Reciprocal space map of the $(10\bar{1}5)$ reflection of a $Sc_{0.14}Al_{0.86}N$/GaN (6 nm, 6 nm) MQW structure (labeled set of equally spaced, vertically stacked peaks). The intensity color scale has units of detected x-ray counts. The maxima corresponding to the 2 µm GaN template and a 100 nm AlN nucleation layer originating from the substrate are also labeled. The instrumental resolution is reflected in the profile of the $(10\bar{1}5)$ GaN reflection. The diagonal streak observed near the GaN peak is an artifact due to the monochromator.

To estimate the charge density in the $Sc_{0.14}Al_{0.86}N$/GaN MQWs, Hall measurements were carried out using the Van Der Pauw geometry in a Quantum Design DynaCool Physical Properties Measurement System (PPMS). The Hall samples were approximately 4 mm by 4 mm with indium contacts at the corners that were annealed at 450°C to ensure ohmic contacts.

The near-infrared intersubband absorption was measured using Fourier transform infrared (FTIR) spectroscopy. These measurements were carried out with a Thermo Scientific Nicolet 8700 spectrometer, equipped with an indium antimonide (InSb) detector and a white light source. To maximize the interaction with the active region, the samples were polished to form parallel 45° facets, facilitating multiple passes of light through the structure. Both s-polarized and p-polarized transmission spectra were recorded, along with their corresponding background spectra. The ISB absorption spectra were subsequently extracted by taking the ratio of the background-normalized p-polarized transmission spectra to the s-polarized transmission spectra and the ISB absorption was calculated per pass for all 50 QWs [62]. The infrared absorption spectra were fitted with Lorentzian functions to extract ISB transition energy and full-width-at-half-maximum linewidth.

Optical Materials EXPRESS

The electronic band structure of $Sc_{0.14}Al_{0.86}N$/GaN MQWs was modeled using the nextnano++ simulation package [64]. Nextnano++ employs the 8-band $\mathbf{k}\cdot\mathbf{p}$ model for each material and solves the Schrodinger and Poisson equations self-consistently. The energy eigenvalues, electronic wavefunctions, and charge density were calculated in the conduction band of a single GaN quantum well with $Sc_{0.14}Al_{0.86}N$ barriers using periodic boundary conditions to simulate the MQW structure. The ISB energies were then corrected for many-body effects in the Local Density Approximation (LDA) [20]. The material parameters for GaN and AlN used in the simulations were sourced from widely accepted references, as cited in Ref. [65]. To model the ScAlN alloys, we considered a hypothetical wurtzite ScN with material parameters detailed in the Supplement 1. The model assumes that $Sc_{0.14}Al_{0.86}N$ is lattice-matched to GaN, with the in-plane lattice constant for ScN (a) set to 3.662 nm. The band alignment between $Sc_xAl_{1-x}N$ and GaN (CBO = 2.1 eV) was taken from recent high-resolution x-ray photoelectron spectroscopy measurements [19,66]. For the polarization and elastic constants of wurtzite ScN, we first used the values proposed by Caro et al [55]. based on DFT calculations, and then adjusted the parameters to fit the experimental data as described in the text below. All other band structure parameters for ScN were set to the values of AlN. We do not expect small changes of these simulation parameters to impact the conclusions of our study.

3. Results and discussion

$Sc_{0.14}Al_{0.86}N$/GaN MQWs demonstrate outstanding ISB absorption in the near-infrared spectral range. Figure 2 summarizes the variation of intersubband transition energy as a function of target QW width for a series of samples grown at a substrate temperature of approximately 525°C. Typical ISB spectra are shown in Fig. 3. As the target QW width increases, the transition energy decreases, showing the expected inverse relationship. The ISB absorption energies span the range from 707 meV to 515 meV for target QW widths from 1.5 nm to 7 nm, respectively. Most notably, ISB absorption in ultra-thin $Sc_{0.14}Al_{0.86}N$/GaN MQWs reaches the highest energy (i.e. shortest wavelength, 1.75 µm) ever reported in Sc-containing MQWs [62]. Moreover, the absorption lines are comparable with or narrower (minimum linewidth 46.5 meV) than all other data for nitrides available in the literature [12].

The ISB absorption is due to electronic transitions between the ground state and the first excited state in the conduction band as illustrated by the band diagram in the inset of Fig. 2. The transition energies are influenced by QW width, barrier width, height of the QW (CBO), sheet electron density, and the tilt of the band structure at the bottom of the QWs due to polarization fields. The expected theoretical dependence of ISBT energies on QW width is shown with solid lines in Fig. 2 for two charge densities. Consistent with our previous findings [62], the ISBT energies in $Sc_{0.14}Al_{0.86}N$/GaN MQWs wider than 3 nm are dominated by the polarization charge mismatch at the well-barrier interface that results in a triangular well profile. In this case, the quantum confinement is set by the ScAlN barrier shown on the right in the inset of Fig. 2, and the GaN conduction band (CB) tilt on the left. As the GaN CB slope decreases linearly with increasing QW width, the ISB transition energy also decreases approximately linearly. Since we assume that $Sc_{0.14}Al_{0.86}N$ is in-plane lattice-matched to GaN, only spontaneous polarization mismatch contributes to the CB slope. Our simulations employed the widely accepted value for GaN spontaneous polarization of -0.034 C/m^2 [65]. The individual contributions of the wurtzite ScN and bowing parameter to the alloy spontaneous polarization can be adjusted as discussed further below, but the overall trend of the experimental ISBT energy for wide QWs is well reproduced by a $Sc_{0.14}Al_{0.86}N$ spontaneous polarization of -0.102 C/m^2. Only for QWs narrower than 3 nm, we expect a rapid increase in ISBT energy due to enhanced confinement from the left-hand barrier (see Figure S1 in Supplement 1).

Incorporating many-body energy corrections into the single-electron model is crucial for accurately calculating ISBT energies in nitride-based QWs. Therefore, the energies simulated

Optical Materials EXPRESS

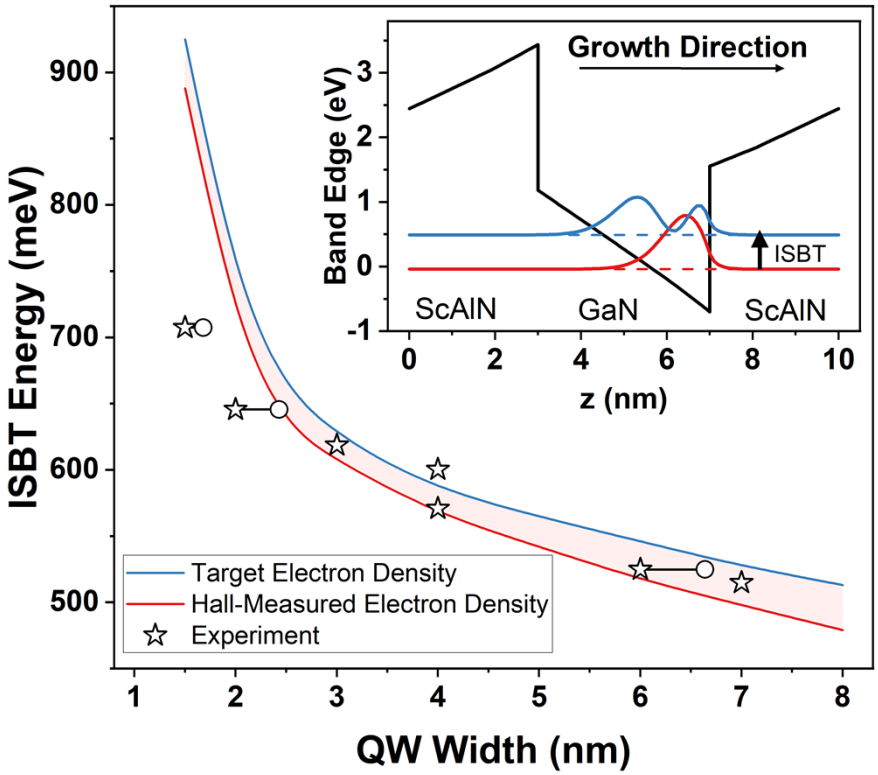

Fig. 2. The effect of QW width on ISB transition energy in $Sc_{0.14}Al_{0.86}N$/GaN MQWs grown at approximately 525°C: experiment (stars and circles) and simulations (lines). Horizontal bars indicate, where available, the range between target QW widths (stars) and average layer thicknesses measured with HAADF-STEM (circle). The measurement errors of the experimental transition energies are smaller than the size of the symbols. The simulated transition energies were corrected for many-body effects using LDA for target (1.6×10^{13} cm^{-2}) and Hall-estimated (1.79×10^{12} cm^{-2}) electron concentrations per QW shown by blue and red curves, respectively. The inset shows the calculated conduction band profile and lowest confined states for a 4 nm GaN QW with 6 nm $Sc_{0.14}Al_{0.86}N$ barriers.

with nextnano++ were corrected for many-body effects using the local density approximation [62]. These corrections account for exchange-correlation energy, depolarization shifts, and excitonic effects. Overall, the transition energies increase with sheet electron concentration in the QWs [67]. Fig. 2 compares experimental data with calculated energies for two different electron densities in the quantum wells: the target sheet electron density per QW (1.6×10^{13} cm^{-2}), and the sheet electron density estimated from Hall measurements (1.79×10^{12} cm^{-2}). The two lines mark the upper and lower bounds for the ISBT energies at each QW width, with the shaded region between the curves representing the range within which the experimental transition energy is predicted to fall. Only minor deviations between the theoretical predictions and the experimental results are observed for QWs wider than 3 nm, likely due to deviations of QW widths from intended target values.

It is important to emphasize that the QW width is a major source of uncertainty in our measurements, especially for the narrowest wells. The differences between target QW widths and the values measured by XRD and HAADF-STEM can be seen in the Supplement 1. XRD analysis accurately estimates the average period thickness (well + barrier) but requires additional

Optical Materials EXPRESS

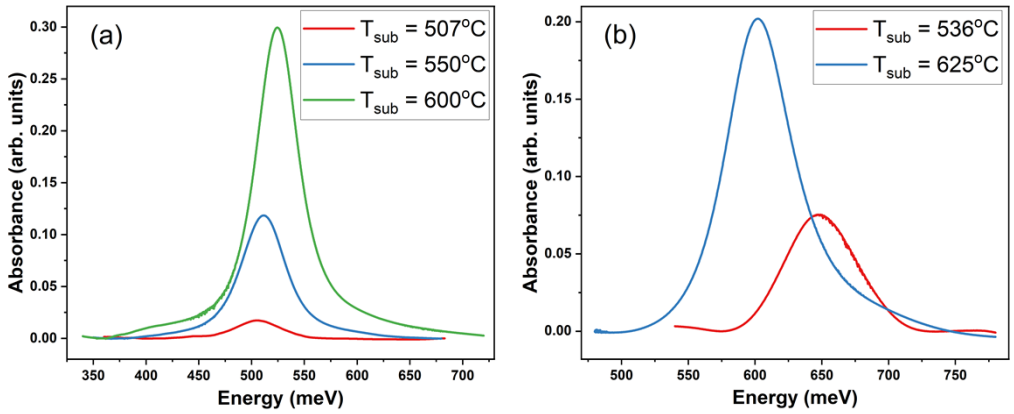

Fig. 3. Intersubband absorption spectra of 50-repeat $Sc_{0.14}Al_{0.86}N$/GaN MQWs grown at different substrate temperatures. ISB absorption dependence on growth temperature for 6 nm QWs (a), and 2 nm QWs (b).

assumptions (i.e. well to barrier thickness ratio inferred from growth times) to extract the QW width. The resulting value is an average over all 50 QWs in the millimeter-size x-ray beam spot. The MBE growth process is typically calibrated with XRD of wide QWs (i.e. period thickness > 10 nm), and therefore the relative deviation of those QWs thicknesses from target values is smaller than for narrow QWs. HAADF-STEM, on the other hand, offers atomic resolution, but then the widths need to be averaged over all QWs for an adequate comparison with the target and XRD values. For this reason, Fig. 2 indicates with horizontal bars the range between target QW widths (stars) and average GaN thicknesses measured by HAADF-STEM (circles), where available. Since deviation of QW thicknesses wider than 3 nm from target values is expected to result in small ISBT energy variation, we conclude that the theoretical model provides a good fit to the experimental data in this width range.

A more pronounced discrepancy between measured and predicted ISBT energies is evident for the ultra-thin (< 2.5 nm) QW samples which exhibit significantly lower transition energies than anticipated by the theoretical model. This inconsistency underscores the challenges associated with growing such thin QWs that are only a few GaN monolayers thick. Understanding this discrepancy requires a careful examination of the interfaces between GaN and ScAlN in narrow QW structures with HAADF-STEM. In contrast to the abrupt interfaces assumed in simulations — where the conduction band edge undergoes sharp steps from GaN to ScAlN as shown in the inset of Fig. 2 — the real structures exhibit interfaces that extend over at least three monolayers (Fig. 1(a)). These interfaces do not affect significantly ISBT energies in wider QWs, but have a dramatic effect in thin QWs, where monolayer thickness fluctuations (±0.26 nm) are expected to lead to ISBT energy variation of more than 50 meV. We have modeled these non-ideal interfaces with a composition varying thin $Sc_xAl_yGa_{1-x-y}N$ interlayer on each side of the GaN and found a strong ISBT energy dependence on the specific structure of the interface. However, it is possible that the fundamental assumptions of our model still do not capture all details of real structures. Calculating the transition energy in the one-dimensional approximation for the average QW width ignores the fact that the GaN layer can only be made of an integer number of GaN monolayers. It also neglects possible confinement due to in-plane conduction band variation. Moreover, modeling the band structure using bulk parameters may be inadequate and an atomistic model may need to be considered. Experimentally, it is apparent that reducing interface roughness is essential for reaching the technologically important 1.55 µm (800 meV) range and can be achieved by optimizing growth conditions.

Optical Materials EXPRESS

Growth temperature plays a pivotal role for interface roughness in MBE growth of MQWs. Consequently, to improve the interface quality and overall optical absorption in $Sc_{0.14}Al_{0.86}N$/GaN MQWs, we investigated the structural and optical properties in these MQWs grown at various substrate temperatures. A series of $Sc_{0.14}Al_{0.86}N$/GaN MQWs were grown at substrate temperatures ranging from 507 to 625°C. The impact of substrate temperature (T_{sub}) on ISB absorption is illustrated in Fig. 3 for two distinct sets of MQWs: one with 6 nm GaN QWs and 6 nm $Sc_{0.14}Al_{0.86}N$ barriers (a), and another with 2 nm GaN QWs and 6 nm $Sc_{0.14}Al_{0.86}N$ barriers (b). In both cases, higher substrate temperatures lead to more intense absorption peaks, most likely due to improved silicon dopant activation. For 6 nm QW structures, the position of the absorption peak does not change significantly with substrate temperature (≈ 500 meV). This suggests that the primary energy transition remains consistent across the samples, with the substrate temperature primarily influencing the peak intensity. In contrast, for the thinner 2 nm QW structures, a significant shift in the absorption peak position towards lower energies (redshift) is observed as the substrate temperature increases from 536°C to 625°C. Consequently, a trade-off between absorption intensity and desired ISBT energy needs to be made by carefully adjusting the substrate temperature depending on the target quantum well thickness.

The reduction of the transition energy in thin MQWs grown at higher temperature can be explained by examining the effect of substrate temperature on QW uniformity and interface roughness. Figures 4(a) and (b) show HAADF-STEM images for two samples with a target QW width of 2 nm, grown at different substrate temperatures, highlighting the structure of the interfaces in each sample. The interface positions, defined as the points of half-maximal intensity between the ScAlN minima and the GaN maxima, are extracted for each pixel column, corresponding to a width of approximately 19 pm. This approach enables the determination of QW widths at different locations within the image, as well as the calculation of the rms roughness of each interface.

The sample grown at 536°C exhibits smooth interfaces with rms comparable to that of the GaN substrate (≈ 0.1 nm) and relatively uniform quantum well thicknesses. In contrast, the sample grown at 625°C shows significantly rougher interfaces with the top of the $Sc_{0.14}Al_{0.86}N$ layers (rms > 0.3 nm) consistently rougher than the top of GaN layers (rms ≈ 0.2 nm). Given that optimal MBE growth conditions for GaN are typically above 700°C, we speculate that ScAlN surface roughening at higher temperature is partially compensated by a smoothing effect of GaN growth. The evolution of the surface roughness at 536°C and 625°C are shown schematically in Figs. 4(c) and 4(d), respectively. As a result of the rougher interfaces at 625°C, the QW thicknesses vary from 1.3 nm to 3.6 nm, with most wells measuring between 2 and 2.6 nm (see Figure S2 in Supplement 1). The presence of GaN regions considerably thicker than the target 2 nm explains the observed redshift in the ISB transition energy. Regions of intermediate contrast are also observed within the ScAlN layers in Fig. 4(b) that are due to either surface roughness in the direction perpendicular to the image or to additional intermixing of the materials resulting in quaternary $Sc_xAl_yGa_{1-x-y}N$ alloys. Clearly, the higher substrate temperature is less than optimal for the growth of narrow ScAlN/GaN MQWs.

Next, we investigate the effect of barrier Sc composition on ISB transition energies. Previously, we reported ISB absorption in $Sc_{0.18}Al_{0.82}N$/GaN MQWs [62]. For each QW width, the ISB absorption occurs at lower energies in QW with $Sc_{0.14}Al_{0.86}N$ barriers compared to QWs with $Sc_{0.18}Al_{0.82}N$ barriers [62]. The change in Sc composition in the alloy impacts the conduction band profile in two primary ways: (1) it influences the conduction band offset (CBO), and (2) it alters the slope of the conduction band due to polarization fields. The change in CBO is relatively small and does not significantly affect the transition energies, as the first two subbands are positioned near the bottom of the quantum wells (inset of Fig. 2). In contrast, polarization fields have a more pronounced impact on transition energies. Since we assume that $Sc_{0.14}Al_{0.86}N$ is lattice-matched to GaN, the conduction band profile and transition energies in

Optical Materials EXPRESS

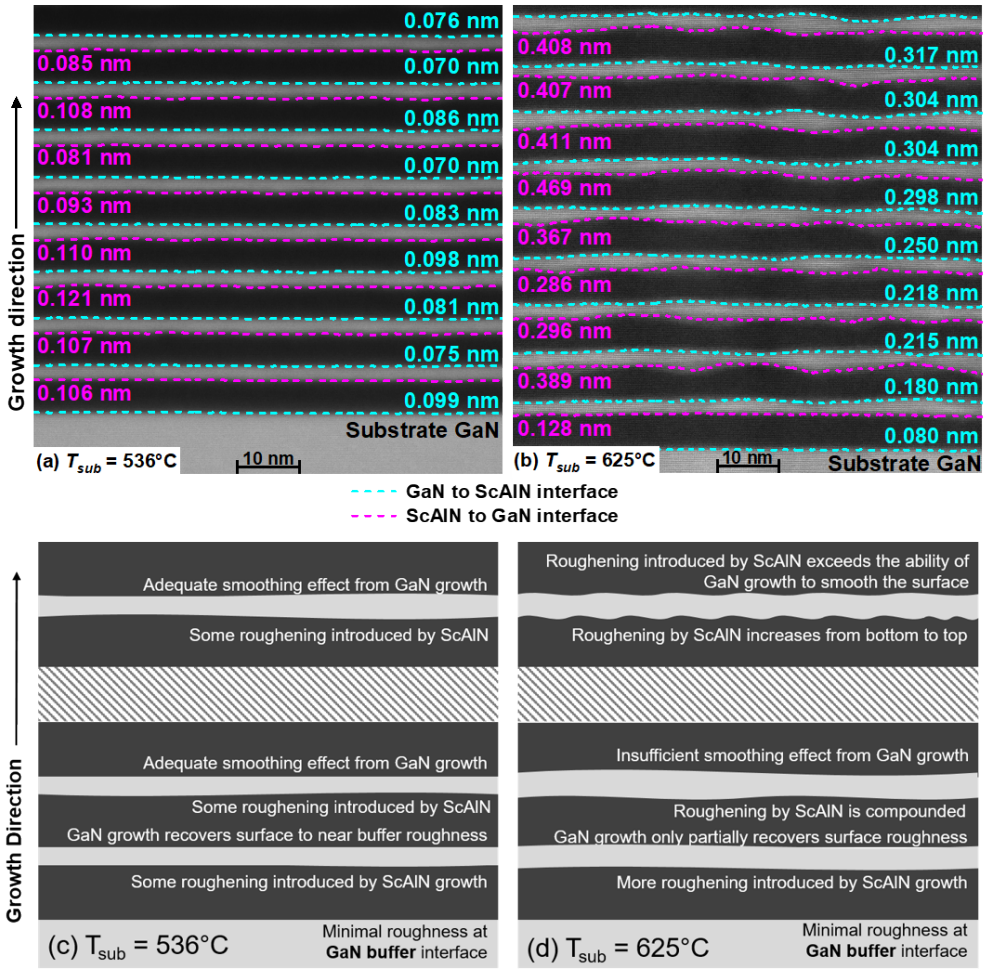

Fig. 4. HAADF-STEM images of 2 nm GaN/6 nm $Sc_{0.14}Al_{0.86}N$ MQW structures grown at (a) T_{sub} = 536°C (sample S2) and (b) T_{sub} = 625°C (Sample S3). Dark regions represent the $Sc_{0.14}Al_{0.86}N$ barriers, while the light regions are GaN well layers. The dashed lines show the locations of the two distinct types of interfaces occurring due to material growth differences: top of GaN (blue), and top of $Sc_{0.14}Al_{0.86}N$ (magenta). The calculated rms roughness values are indicated with corresponding colors next to each interface. Schematics of the surface roughness evolution during MBE growth at T_{sub} = 536°C (c), and T_{sub} = 625°C (d).

$Sc_{0.14}Al_{0.86}N$/GaN MQWs are determined only by spontaneous polarization. In the non-lattice-matched $Sc_{0.18}Al_{0.82}N$/GaN structures, however, the strain-induced piezoelectric polarization also contributes to the band structure. The interplay between these components determines composition dependence of ISBT energies.

Figure 5(a) shows the expected theoretical dependence of polarization constants in $Sc_xAl_{1-x}N$ on Sc composition in the x = 0 - 0.3 range. The plot includes spontaneous polarization (P_{sp}), piezoelectric polarization (P_{pz}), and total polarization. The detailed equations governing these parameters are given in the Supplement 1s. The dashed lines represent the polarization constants calculated using the parameters proposed by Caro et al. [55], referred to as 'default' parameters hereon. The magnitude of the spontaneous polarization is expected to be larger than piezoelectric

Optical Materials EXPRESS

polarization at all compositions. The piezoelectric polarization is proportional to strain and changes sign at the lattice-matching composition x = 0.14. For barriers with Sc compositions above 0.14, such as $Sc_{0.18}Al_{0.82}N$/GaN MQWs, the compressive strain results in piezoelectric polarization fields that are oriented in the opposite direction of the spontaneous polarization, effectively reducing the spontaneous polarization. Since ISBT energies depend on conduction band slope, the key trend to note here is the behavior of the total polarization. For the parameters proposed by Caro et al. [55], the magnitude of the total polarization decreases continuously with increasing Sc composition. This would correspond to a decrease of ISBT energy when x increases from 0.14 to 0.18 (Fig. 5(b)), in disagreement with our experimental results.

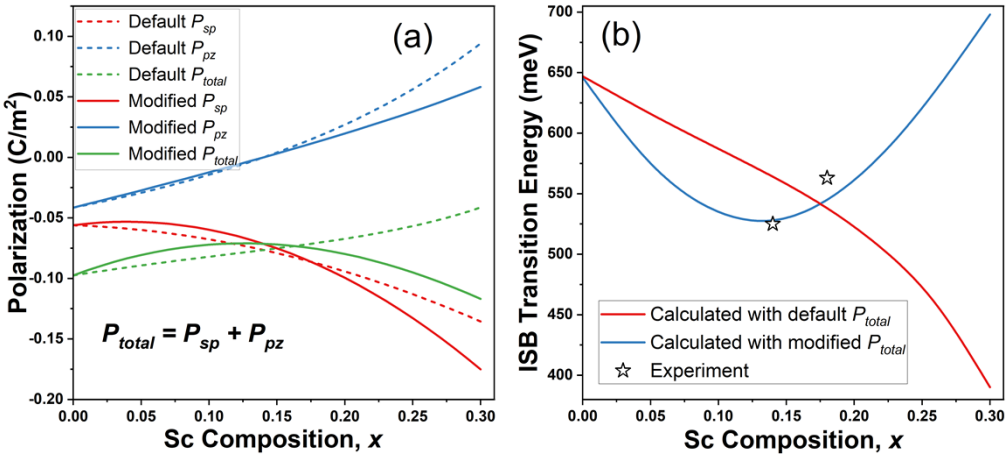

Fig. 5. (a) Calculated spontaneous, piezoelectric, and total polarization for $Sc_xAl_{1-x}N$ plotted as a function of Sc composition (x). The curves calculated with parameters derived by Caro et al [55]. from theoretical simulations are plotted using dashed lines. The solid lines show the spontaneous, piezoelectric, and total polarization calculated with the modified parameters proposed in this work. (b) Simulated ISB transition energy of a 6 nm QW with 6 nm ScAlN barriers as a function of Sc composition calculated using the default [55] and modified polarization parameters proposed in this work. The stars denote experimental ISBT energies.

To fit all the available experimental ISB data, we adjusted the spontaneous polarization (P_{sp}) and piezoelectric coefficients (e_{33}) for the hypothetical wurtzite ScN and the corresponding bowing parameters (see proposed values in Supplement 1). The two parameters corresponding to spontaneous polarization are not independent, but are constrained to give the net spontaneous polarization of the lattice-matched $Sc_{0.14}Al_{0.84}N$ that best fit the experimental data in Fig. 2(-0.102 C/m^2). The solid lines in Fig. 5(a) show the polarization components calculated using these 'modified' parameters. In this case the magnitude of the spontaneous polarization increases faster, while the piezoelectric component increases slower for x from 0.14 to 0.18 than proposed by Caro et al [55]. As a result, the total polarization follows a non-monotonic trend (Fig. 5(a) green solid line). Its magnitude starts at 0.097 C/m^2 for pure AlN, decreases to a minimum of approximately 0.07 C/m^2 around 13% Sc composition, and then continuously increases up to $x = 0.3$. Most importantly, this net increase of the total polarization magnitude ultimately leads to a larger ISBT energy in $Sc_{0.18}Al_{0.82}N$/GaN compared to $Sc_{0.14}Al_{0.86}N$/GaN MQWs (Fig. 5(b)). This model can be further validated by growing a series of $Sc_xAl_{1-x}N$/GaN MQWs with a fixed quantum well width, and increasing the Sc composition beyond 0.18. We plan to continue investigating the polarization parameters of ScAlN, as they are critical for accurately modeling the material band-structure, particularly for its application in optoelectronic and electronic devices.

Optical Materials EXPRESS

4. Conclusions

We demonstrated outstanding performance of MBE-grown $Sc_{0.14}Al_{0.86}N$/GaN MQWs lattice-matched to c-plane GaN for near-infrared intersubband absorption across a broad spectral range. Experimental ISB absorption energies span the range from 709 meV to 515 meV for QW widths ranging from 1.5 nm to 7 nm, respectively. The measured ISB absorption linewidths are among the narrowest reported for nitride semiconductors in this energy range. The MBE growth temperature was found to have a major impact on ISB absorption in ScAlN/GaN MQWs. Higher growth temperatures (> 600°C) were found to improve absorption intensity and linewidth for all QWs. In ultra-thin QWs (2 nm), though, the highest growth temperatures resulted in significantly lower transition energies due to increased interface roughness and ensuing GaN thickness non-uniformity.

This study also explored the role of spontaneous and piezoelectric polarization in determining ISB transition energies in Sc-containing nitrides. Experimental ISB results indicate that the spontaneous polarization of the ScAlN/GaN heterostructure increases faster with Sc-composition than previously suggested by theoretical calculations. We propose alternative spontaneous and piezoelectric coefficients that accurately reproduce all available near-infrared experimental data for quantum wells wider than 3 nm. However, the model breaks down in ultra-thin QWs likely because it neglects the critical role of interfaces. Overall, this study advances the understanding of ScAlN/GaN heterostructures, demonstrating the potential of this material system for novel photonic devices. Future efforts will focus on targeting the telecommunications wavelength of 1.55 µm and further enhancing near-infrared absorption in ScAlN/GaN MQWs by optimizing MBE growth conditions. Moreover, to refine material band-structure models, we will explore the polarization parameters of $Sc_xAl_{1-x}N$ for higher Sc-compositions ($x > 0.18$).

Funding. National Science Foundation (DMR-2004462, DMR-2414283).

Acknowledgment. We acknowledge support from the National Science Foundation (NSF). Z. U. A., G. G., and O.M. acknowledge partial support from NSF awards DMR-2004462 and DMR-2414283. All STEM imaging and analyses were performed at the Electron Microscopy Facility at the Birck Nanotechnology Center, Purdue University.

Disclosures. The authors declare no conflicts of interest.

Data availability. Data underlying the results presented in this paper are available within the article.

Supplemental document. See Supplement 1 for supporting content.

References

1. Z. C. Feng, *III-Nitride Semiconductor Materials* (Imperial Publishing Press, 2006).
2. P. Wang, D. Wang, S. Mondal, *et al.*, "Dawn of nitride ferroelectric semiconductors: from materials to devices," Semicond. Sci. Technol. **38**(4), 043002 (2023).
3. V. Yoshioka, J. Lu, Z. Tang, *et al.*, "Strongly enhanced second-order optical nonlinearity in CMOS-compatible $Al_{1-x}Sc_xN$ thin films," APL Mater. **9**(10), 101104 (2021).
4. D. Wang, P. Wang, S. Mondal, *et al.*, "An epitaxial ferroelectric ScAlN/GaN heterostructure memory," Adv. Electron. Mater. **8**(9), 2200005 (2022).
5. F. Yang, G. Yang, D. Wang, *et al.*, "Domain control and periodic poling of epitaxial ScAlN," Appl. Phys. Lett. **123**(10), 101103 (2023).
6. F. Chen, X. Ji, S. P. Lau, *et al.*, "Recent progress in group III-nitride nanostructures: From materials to applications," Sci. Eng. Rep. **142**, 100578 (2020).
7. S. Nakamura, M. Senoh, N. Iwasa, *et al.*, "High-brightness InGaN blue, green and yellow light-emitting diodes with quantum well structures," J. Appl. Phys. **34**(7A), L797 (1995).
8. S. Nakamura, M. Senoh, S. Nagahama, *et al.*, "InGaN-based multi-quantum-well-structure laser diodes," J. Appl. Phys. **35**(1B), L74 (1996).
9. W. S. Wong, T. Sands, N. W. Cheung, *et al.*, "In_xGa_{1-x}Nlight emitting diodes on Si substrates fabricated by Pd-In metal bonding and laser lift-off," Appl. Phys. Lett. **77**(18), 2822–2824 (2000).
10. O. Ambacher, "Growth and applications of Group III-nitrides," J. Phys. D: Appl. Phys. **31**(20), 2653–2710 (1998).
11. H. Fu and Y. Zhao, in *Nitride Semiconductor Light-Emitting Diodes (LEDs)* (2nd Edition), pp. 299–325 (2018).
12. M. Beeler, E. Trichas, and E. Monroy, "III-nitride semiconductors for intersubband optoelectronics: a review," Semicon. Sci. Technol. **28**(7), 074022 (2013).

Optical Materials EXPRESS

13. D. H. Mudiyanselage, D. Wang, Y. Zhao, *et al.*, "Intersubband transitions in nonpolar and semipolar III-nitrides: Materials, devices, and applications," J. Appl. Phys. **131**(21), 210901 (2022).
14. D. Hofstetter, S. -S. Schad, H. Wu, *et al.*, "GaN/AlN-based quantum-well infrared photodetector for 1.55 μm," Appl. Phys. Lett. **83**(3), 572–574 (2003).
15. H. Durmaz, D. Nothern, G. Brummer, *et al.*, "Terahertz intersubband photodetectors based on semi-polar GaN/AlGaN heterostructures," Appl. Phys. Lett. **108**(20), 201102 (2016).
16. R. Kohler, A. Tredicucci, F. Beltram, *et al.*, "Terahertz semiconductor-heterostructure laser," Nature **417**(6885), 156–159 (2002).
17. B. Williams, "Terahertz quantum-cascade lasers," Nat. Photonics **1**(9), 517–525 (2007).
18. H.C. Liu and F. Capasso, *Intersubband Transitions in Quantum Wells: Physics and Device Applications I*, (Academic Press, 2000).
19. D. Wang, D. Wang, P. Zhou, *et al.*, "On the surface oxidation and band alignment of ferroelectric Sc0.18Al0.82N/GaN heterostructures," Appl. Surf. Sci. **628**, 157337 (2023).
20. T. Nguyen, B. Dzuba, Y. Cao, *et al.*, "Mid-infrared intersubband absorption in strain-balanced non-polar (In)AlGaN/InGaN multi-quantum wells," Opt. Mater. Express **11**(9), 3284–3297 (2021).
21. O. Malis, T. Nguyen, Y. Cao, *et al.*, "Novel nitride quantum structures for infrared sensing," Proc. SPIE **12009**, 120090B (2022).
22. A. Ajay and E. Monroy, in *Mid-infrared Optoelectronics, Materials, Devices, and Applications* (Woodhead Publishing Series in Electronic and Optical Materials, 2020), pp. 539–565.
23. J. Heber, C. F. Gmachl, H. M. Ng, *et al.*, "Comparative study of ultrafast intersubband electron scattering times at ∼1.55 μm wavelength in GaN/AlGaN heterostructures," Appl. Phys. Lett. **81**(7), 1237–1239 (2002).
24. B. Dzuba, T. Nguyen, A. Sen, *et al.*, "Elimination of remnant phases in low-temperature growth of wurtzite ScAlN by molecular-beam epitaxy," J. Appl. Phys. **132**(17), 175701 (2022).
25. M. Kuball, M. Ťapajna, R. J. T. Simms, *et al.*, "AlGaN/GaN HEMT device reliability and degradation evolution: Importance of diffusion processes," Micro. Rel. **51**(2), 195–200 (2011).
26. J. A. del Alamo and J. Joh, "GaN HEMT reliability," Micro. Rel. **49**(9-11), 1200–1206 (2009).
27. S. Choi, F. Wu, R. Shivaraman, *et al.*, "Observation of columnar microstructure in lattice-matched InAlN/GaN grown by plasma assisted molecular beam epitaxy," Appl. Phys. Lett. **100**(23), 232102 (2012).
28. L. van Deurzen, T. -S. Nguyen, J. Casamento, *et al.*, "Epitaxial lattice-matched AlScN/GaN distributed Bragg reflectors," Appl. Phys. Lett. **123**(24), 241104 (2023).
29. R. Kumar, G. Gopakumar, Z. U. Abdin, *et al.*, "Pinpointing lattice-matched conditions for wurtzite $Sc_xAl_{x1-x}N$/GaN heterostructures with x-ray reciprocal space analysis," Appl. Phys. Lett. **125**, 5 (2024).
30. G. Wingqvist, F. Tasnádi, A. Zukauskaite, *et al.*, "Increased electromechanical coupling in w−$Sc_xAl_{1-x}N$," Appl. Phys. Lett. **97**(11), 112902 (2010).
31. W. Wang, P. M. Mayrhofer, X. He, *et al.*, "High performance AlScN thin film based surface acoustic wave devices with large electromechanical coupling coefficient," Appl. Phys. Lett. **105**(13), 133502 (2014).
32. W. B. Wang, Y. Q. Fu, J. J. Chen, *et al.*, "AlScN thin film based surface acoustic wave devices with enhanced microfluidic performance," J. Micromech. Microeng. **26**(7), 075006 (2016).
33. R. Dargis, A. Clark, A. Ansari, *et al.*, "Single-crystal multilayer nitride, metal, and oxide structures on engineered silicon for new-generation radio frequency filter applications," Phys. Stat. Sol. (a) **217**(7), 1900813 (2020).
34. A. Ding, L. Kirste, Y. Lu, *et al.*, "Enhanced electromechanical coupling in SAW resonators based on sputtered non-polar Al0.77Sc0.23N 112 thin films," Appl. Phys. Lett. **116**(10), 101903 (2020).
35. V. J. Gokhale, B. P. Downey, M. T. Hardy, *et al.*, in *2020 IEEE 33rd International Conference on Micro Electro Mechanical Systems (MEMS)* (IEEE, Vancouver, BC, Canada, 2020), pp. 1262–1265.
36. M. T. Hardy, B. P. Downey, D. J. Meyer, *et al.*, "Epitaxial ScAlN etch-stop layers grown by molecular beam epitaxy for selective etching of AlN and GaN," IEEE Trans. Semicond. Manufact. **30**(4), 475–479 (2017).
37. S. Zhang, D. Holec, W. Y. Fu, *et al.*, "Tunable optoelectronic and ferroelectric properties in Sc-based III-nitrides," J. Appl. Phys. **114**(13), 133510 (2013).
38. P. Wang, D. Wang, N. M. Vu, *et al.*, "Fully epitaxial ferroelectric ScAlN grown by molecular beam epitaxy," Appl. Phys. Lett. **118**(22), 223504 (2021).
39. S. Barth, H. Bartzsch, D. Gloess, *et al.*, "Influence of process parameters on properties of piezoelectric AlN and AlScN thin films for sensor and energy harvesting applications," Proc. SPIE **9517**, 951704 (2015).
40. R. Deng, S. R. Evans, and D. Gall, "Bandgap in $Al1-_xSc_xN$," Appl. Phys. Lett. **102**(11), 112103 (2013).
41. N. Farrer and L. Bellaiche, "Properties of hexagonal ScN versus wurtzite GaN and InN," Phys. Rev. B **66**(20), 201203 (2002).
42. S. Zhang, W. Y. Fu, D. Holec, *et al.*, "Elastic constants and critical thicknesses of ScGaN and ScAlN," J. Appl. Phys. **114**(24), 243516 (2013).
43. O. Ambacher, B. Christian, N. Feil, *et al.*, "Wurtzite ScAlN, InAlN, and GaAlN crystals, a comparison of structural, elastic, dielectric, and piezoelectric properties," J. Appl. Phys. **130**(4), 045102 (2021).
44. D. F. Urban, O. Ambacher, and C. Elsässer, "First-principles calculation of electroacoustic properties of wurtzite (Al,Sc)N," Phys. Rev. B **103**(11), 115204 (2021).
45. F. Tasnádi, B. Alling, C. Höglund, *et al.*, "Origin of the anomalous piezoelectric response in Wurtzite Sc_xAl_{1-x}," Phys. Rev. Lett. **104**(13), 137601 (2010).

Optical Materials EXPRESS

46. M. T. Hardy, B. P. Downey, N. Nepal, *et al.*, "Epitaxial ScAlN grown by molecular beam epitaxy on GaN and SiC substrates," Appl. Phys. Lett. **110**(16), 162104 (2017).
47. P. Wang, D. A. Laleyan, A. Pandey, *et al.*, "Molecular beam epitaxy and characterization of wurtzite $Sc_xAl_{1-x}N$," Appl. Phys. Lett. **116**(15), 151903 (2020).
48. J. Casamento, H. Lee, C. S. Chang, *et al.*, "Strong effect of scandium source purity on chemical and electronic properties of epitaxial $Sc_xAl_{1-x}N$/GaN heterostructures," APL Mater. **9**(9), 091106 (2021).
49. J. Casamento, H. Xing, and D. Jena, "Oxygen incorporation in the molecular beam epitaxy growth of $Sc_xGa_{1-x}N$ and $Sc_xAl_{1-x}N$," Phys. Status Solidi B **257**(4), 1900612 (2020).
50. J. Casamento, T. -S. Nguyen, Y. Cho, *et al.*, "Transport properties of polarization-induced 2D electron gases in epitaxial AlScN/GaN heterojunctions," Appl. Phys. Lett. **121**(19), 192101 (2022).
51. M. T. Hardy, E. N. Jin, N. Nepal, *et al.*, "Control of phase purity in high scandium fraction heteroepitaxial ScAlN grown by molecular beam epitaxy," Appl. Phys. Express **13**(6), 065509 (2020).
52. K. Frei, R. Trejo-Hernández, S. Schütt, *et al.*, "Investigation of growth parameters for ScAlN-barrier HEMT structures by plasma-assisted MBE," Jpn. J. Appl. Phys. **58**(SC), SC1045 (2019).
53. S. M. Knoll, S. K. Rhode, S. Zhang, *et al.*, "Defects in epitaxial ScGaN: Dislocations, stacking faults, and cubic inclusions," Appl. Phys. Lett. **104**(10), 101906 (2014).
54. M. A. Moram and S. Zhang, "ScGaN and ScAlN: emerging nitride materials," J. Mater. Chem. A **2**(17), 6042–6050 (2014).
55. M. A. Caro, S. Zhang, T. Riekkinen, *et al.*, "Piezoelectric coefficients and spontaneous polarization of ScAlN," J. Phys.: Condens. Matter **27**, 245901 (2015).
56. J. Casamento, H. Lee, T. Maeda, *et al.*, "Epitaxial $Sc_xAl_{1-x}N$ on GaN exhibits attractive high-K dielectric properties," Appl. Phys. Lett. **120**(15), 152901 (2022).
57. A. J. Green, J. K. Gillespie, R. C. Fitch, *et al.*, "ScAlN/GaN High-Electron-Mobility Transistors With 2.4-A/mm Current Density and 0.67-S/mm Transconductance," IEEE Electron Device Lett. **40**(7), 1056–1059 (2019).
58. P. Wang, D. Wang, B. Wang, *et al.*, "N-polar ScAlN and HEMTs grown by molecular beam epitaxy," Appl. Phys. Lett. **119**(8), 082101 (2021).
59. A. J. Green, N. Moser, N. C. Miller, *et al.*, "RF Power Performance of Sc(Al,Ga)N/GaN HEMTs at Ka-Band," IEEE Electron Device Lett. **41**(8), 1181–1184 (2020).
60. T. E. Kazior, E. M. Chumbes, B. Schultz, *et al.*, in *2019 IEEE MTT-S International Microwave Symposium (IMS)*, Boston, MA, USA, pp. 1136–1139 (2019).
61. D.-P. Yang, X.-G. Tang, Q.-J. Sun, *et al.*, Mater. Horiz. **11**, 282 (2024).
62. G. Gopakumar, Z. U. Abdin, R. Kumar, *et al.*, "Conduction-band engineering of polar nitride semiconductors with wurtzite ScAlN for near-infrared photonic devices," J. Appl. Phys. **135**(16), 16 (2024).
63. S. Gozu, T. Mozume, H. Kuwatsuka, *et al.*, "InGaAs/AlAs/InAlAs coupled double quantum wells for intersubband transition devices operating at 1550nm," J. Cryst. Growth **378**, 134–136 (2013).
64. S. Birner, T. Zibold, T. Andlauer, *et al.*, "Nextnano: general purpose 3-D simulations," IEEE Trans. Electron. Devices **54**(9), 2137–2142 (2007).
65. I. Vurgaftman and J. R. Meyer, "Band parameters for nitrogen-containing semiconductors," J. Appl. Phys. **94**(6), 3675–3696 (2003).
66. E. N. Jin, M. T. Hardy, A. L. Mock, *et al.*, "Band Alignment of $Sc_xAl_{1-x}N$/GaN Heterojunctions," ACS Appl. Mater. Interfaces **12**(46), 52192–52200 (2020).
67. P. K. Kandaswamy, F. Guillot, E. Bellet-Amalric, *et al.*, "GaN/AlN short-period superlattices for intersubband optoelectronics: A systematic study of their epitaxial growth, design, and performance," J. Appl. Phys. **104**(9), 093501 (2008).

128.210.107.131 on 2025-01-08 15:21:587